Metals and Materials International (2024) 30:517–532
https://doi.org/10.1007/s12540-023-01516-5

# Non-basal Slips Mediated Dynamic Recrystallization Promote Synergistic Strengthening and Toughening of Centrifugal Casting Mg–1.1Mn–0.5Al Alloy via High Strain Rolling

Fanxiao Kong[1,2] · Huizhen Feng[3] · Hao Chen[1,4] · Yini Lin[1] · Yongxin Wang[1] · Weidong Xie[1] · Guobing Wei[1] · Yan Yang[1] · Xiaodong Peng[1]

Received: 14 June 2023 / Accepted: 29 July 2023 / Published online: 16 September 2023


## Abstract

The synergy of excellent yield strength and ductility has always been a dilemma for conventional rolled magnesium alloys. In this paper, the contributions of alloying elements, deformation twinning and recrystallization to strengthening and toughening of the high strain rolled Mg–1.1Mn–0.5Al (wt%) alloys with variable rolling passes (1, 2, 4 and 7) at low temperature (473 K) were revealed. The results showed that the pyramidal < c + a > slips mediated dynamic recrystallization was prone to promote synergistic strengthening and toughening of the high strain rolled Mg–1.1Mn–0.5Al alloy. The progressive microstructure evolution was characterized with increasing rolling passes by the dominant $\{10\bar{1}2\}$ tension twins, the balanced distribution of $\{10\bar{1}2\}, \{10\bar{1}1\}, \{10\bar{1}3\}, \{10\bar{1}1\}-\{10\bar{1}2\}, \{10\bar{1}3\}-\{10\bar{1}2\}$ and $\{10\bar{1}2\}-\{10\bar{1}2\}$ multi-system twins, the mixed twinning dynamic recrystallization, discontinuous dynamic recrystallization, continuous dynamic recrystallization and the complete recrystallization grains, finally resulting in significant grain refinement to 4.72 μm. It was experiment confirmed that the massive evenly distributed compression twins accompanied by the high < c + a > slips activity were able to coordinate local plastic deformation with each other so as to accommodate high strain rolling, promote strain softening effect and accelerated recrystallization rather than become a source of cracks during high strain rate rolling. Thanks to the micro and nano sized α-Mn and $Al_8Mn_5$ precipitates, which brought out an activation of non-basal slip and accelerated recrystallization additively, the recrystallized Mg–1.1Mn–0.5Al alloy with excellent yield strength (~ 311 MPa), ultimate tensile strength (~ 378 MPa) and fracture elongation (~ 20.4%) were obtained via 7 passes rolling without annealing.

**Keywords** Mg–Mn–Al · Strength-ductility synergy · High strain rate rolling · Low temperature · Recrystallization

## 1 Introduction

Due to lower density, higher specific strength, excellent damping and electromagnetic shielding performance, magnesium alloy has been considered one of the most potential metal structural materials in aerospace, national defense and transportation industries [1–4]. As a key component, Mg alloy ring parts play a decisive role in the reliability, stability and handling of the overall equipment. However, fewer activated slip systems and its resulting poor plastic workability of the Mg alloys seriously limit its wide application [5]. The inefficiency and easy cracking tendency of Mg alloy rings, formed by conventional process of successive casting, multiple forging, punching and multi pass rolling, have been always criticized [6]. Compared with gravity casting, centrifugal casting is more suitable for the forming of ring parts, which exhibit fine grains,

✉ Weidong Xie
xieweidong2019@cqu.edu.cn

✉ Guobing Wei
guobingwei@cqu.edu.cn

1 National Key Laboratory of Advanced Casting Technologies, College of Materials Science and Engineering, Chongqing University, Chongqing 400044, China

2 School of Mechanical and Automotive Engineering, Guangxi University of Science and Technology, Liuzhou 545006, China

3 Chongqing Changan Automobile Company Limited, Chongqing 400044, China

4 Institute of Metallic Biomaterials, Helmholtz-Zentrum Hereon, Max-Planck-Str. 1, 21502 Geesthacht, Germany

improving strength and better ductility [7]. The high strain rolling (HSR) of centrifugal casting rings reduces the intermediate plastic deformation process of multiple forging and punching, resulting in basal texture weakening and avoiding potential forging crack [8]. As one of severe plastic deformation (SPD) machining methods, HSR is an effective processing way for synergistic strengthening and toughening of Mg alloys. The rolled Mg–1.8Al–1.8Ca sheets at 573 K by single pass reduction of 78% exhibited improving mechanical properties for the YS of 298 MPa, UTS of 319 MPa and FE of 6% [9]. The YS, UTS and FE of the HSRed Mg–8.8Gd–3.4Y–1Zn–0.8Mn alloy at 723 K was 318 MPa, 434 MPa and 10.7%, respectively [10].

Generally, the rolled Mg alloys are prone to forming a strong basal texture, which causes anisotropy of stretching and compression. High strain rate plastic deformation at low temperature is conducive to reducing rolling passes, weakening basal texture and avoiding yield asymmetry [11]. However, due to the lack of activated slip system, it is difficult for most Mg alloys to be rolled at low temperature. Mn element, which can reduce the cross-slip energy barrier and help to open non-basal slip of magnesium alloys, is considered as a beneficial element for refining grain and improving ductility [12]. Al element can significantly increase the CRSS of basal slip, produce strong solution strengthening, and improve the yield strength of Mg alloys [13]. It was reported that the α-Mn and $Al_8Mn_5$ particles increased dynamic recrystallization (DRX) nucleation ratio induced by particle stimulation nucleation (PSN) mechanism, and inhibited grain growth by pinning dislocation [14]. As-extruded Mg–1.3Al–0.4Mn–0.3Ca alloy exhibited improving yield strength (YS) of 287 MPa, ultimate tensile strength (UTS) of 343 MPa and fracture elongation (FE) of 20% [15]. The YS of Mg–0.6Mn–0.5Al–0.5Zn–0.4Ca alloy increased to 403 MPa after extrusion and rotary forging [16]. With the addition of 1.0 wt% Mn element, the YS of Mg–Zn–Al–xMn alloy was significantly enhanced by 39 MPa [17]. Therefore, Mg–Mn–Al alloys, which present excellent plasticity, corrosion resistance and economy, are considered to be an easily rolled wrought alloy [18]. However, researches on high strain rate rolling of centrifugal casting Mg–Mn–Al alloys at low temperature are still rarely reported.

In this paper, the centrifugal casting Mg–1.1Mn–0.5Al alloy were prepared and then rolled to variable accumulative strain with single pass 20% reduction at 473 K. Due to activation of pyramidal < c + a > slips, local strain coordination induced by compression twins and accelerated recrystallization, the excellent yield strength and ductility were simultaneously obtained via high strain rolling without further annealing. Meanwhile, the microstructure evolution, strengthening and toughening mechanism of the HSRed Mg–1.1Mn–0.5Al alloys were discussed.

## 2 Experimental Procedures

The commercial raw materials of pure Mg (99.9 wt%), pure Al (99.9 wt%) and Mg-3Mn (wt%) were used to fabricate Mg–1.1Mn–0.5Al alloy. The alloys were melted under the protection of $CO_2$ and $SF_6$ gas mixture in a special well resistance furnace for magnesium alloy. After uniform stirring and slag removal at 973 K, the melt was cast into a rotating horizontal centrifugal casting mold preheated at 523 K for 30 min and eventually formed rings with inner diameter of 40 mm, outer diameter of 90 mm and height of 120 mm. The mold centrifugal speed was kept constant at 600 r/min during pouring and solidification process. After solidification, the casting rings were water chilled to about 373 K and then naturally air cooled to room temperature.

The castings were homogenized at 673 K for 12 h, followed by water chilling to about 373 K and then cut into slabs with thickness of 24 mm. The cut slabs were held at 473 K for 30 min, and then rolled with single pass reduction of 20% on a double-high rolling mill. All the samples were kept at 473 K for 10 min at intervals of each rolling pass. The rollers were kept at room temperature throughout the rolling process. The final rolled samples were cooled immediately in hot water to about 373 K. The final thickness, cumulative reduction and average strain rate of the rolled samples are shown in Table 1. The average strain rate of rolling was calculated as following [19]:

$$\dot{\varepsilon} = \frac{2V\sqrt{\Delta h/R}}{H+h} \tag{1}$$

where $\dot{\varepsilon}$ is average strain rate of rolling, $V$ is roller linear velocity of constant 1.78 m/s, $R$ is the radius of the roller equal to 85 mm, $\Delta h$ is the single pass reduction, $H$ and $h$ are the thickness of the sheet before and after rolling. According

**Table 1** Final thickness, cumulative reduction and average strain rate of the HSRed alloys

| Rolling passes | Thickness, mm | Cumulative reduction (%) | Strain rate $\dot{\varepsilon}$, $s^{-1}$ |
|---|---|---|---|
| 0 | 24.0 | 0 | – |
| 1 | 19.2 | 20 | 19.6 |
| 2 | 14.4 | 40 | 22.5 |
| 3 | 12.0 | 50 | 24.8 |
| 4 | 9.6 | 60 | 27.7 |
| 5 | 7.7 | 68 | 30.9 |
| 6 | 6.1 | 75 | 34.7 |
| 7 | 4.9 | 80 | 38.8 |

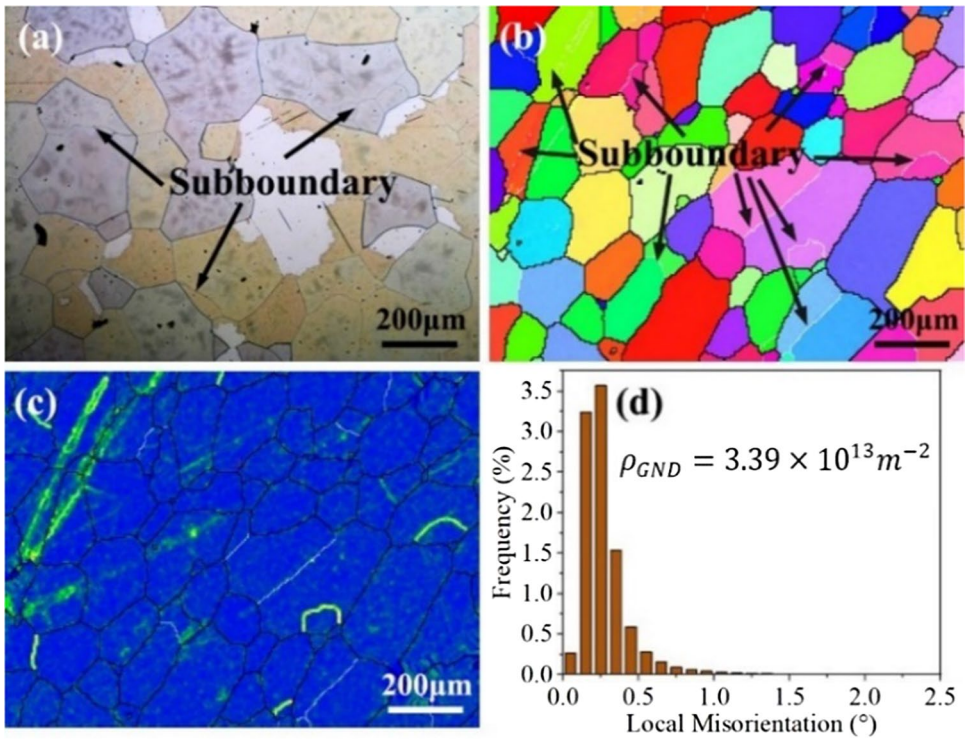


**Fig. 1** Micrographs of the centrifugation casting alloy: **a** OM, **b** IPF, **c** local misorientation and **d** corresponding KAM distribution maps

to the calculated results, $\dot{\varepsilon}$ increases from 19.6 to 38.8 $s^{-1}$ with the increasing rolling passes, which is much higher than that (9.1–11.3 $s^{-1}$) of other conventional rolled magnesium alloys [4, 19].

The microstructure was observed by Olimpus PMG3 optical microscopy (OM), analyzed by FEI Nova 400 scanning electron microscopy (SEM) at 20 kV. The electron backscatter diffraction (EBSD) analysis was performed using JEOL JSM-7800F Field emission scanning tunneling electron microscope with the operating voltage of 20 kV, the beam current of 15 μA and the scanning step of 0.5 μm. The transmission electron microscope (TEM) and scanning transmission electron microscope (STEM) were observed using a Talos F200S microscopy operated at 200 kV. The alloying elements were determined by XRF-1800 X-ray fluorescence spectrometer. Phase analysis was carried out by D/Max-2500PC X-ray diffractometer with test voltage of 40 kV and current of 0.15 A. Mechanical tensile properties of the rectangular section specimens were tested on CMT-5105 electronic universal testing machine with a constant strain rate of $10^{-3}$ $s^{-1}$.

## 3 Results

### 3.1 Microstructure

Figure 1 show the optical microstructure (OM), inverse pole figure (IPF), local misorientation and corresponding kernel average misorientation (KAM) distribution maps of the centrifugal casting Mg–1.1Mn–0.5Al alloys. In the IPF maps, the high angle grain boundaries (HAGBs, $\theta \geq 15°$) and the low angle grain boundaries (LAGBs, $2° \leq \theta < 15°$) were marked with black line and white line, respectively. Different from gravity casting alloy [13], some subcrystalline structure appeared in the grain interior of the centrifugal casting alloys. Generally, the generation of subcrystalline is usually due to the dislocation slip, plugging, rearrangement and merging during the plastic deformation of the alloys. Hence, the corresponding local misorientation maps was given to quantitatively confirm dislocation density of the centrifugally cast alloys. The geometrically necessary dislocation (GND) density was calculated by [20]:

$$\rho_{GND} = 2\Delta\theta_i / \mu b \tag{2}$$

where $\rho_{GND}$ is average GND density, $\Delta\theta_i$ is mean value of KAM, $\mu$ is EBSD step size and $b$ is the Burgers vector (0.32 nm in use). Consequently, the calculated GND density of centrifugal castings are $3.39 \times 10^{13} m^{-2}$. Centrifugal casting melt was subjected to a combination of centrifugal force, viscous force, inertial force and repulsive force [7, 21], which caused intergranular stress during solidification of centrifugal castings with high-speed spiral motion and activated dislocation slips. Considering the high frequency vibration of the centrifugal casting mold during rotation, this is beneficial to the grain refinement of the centrifugal castings.

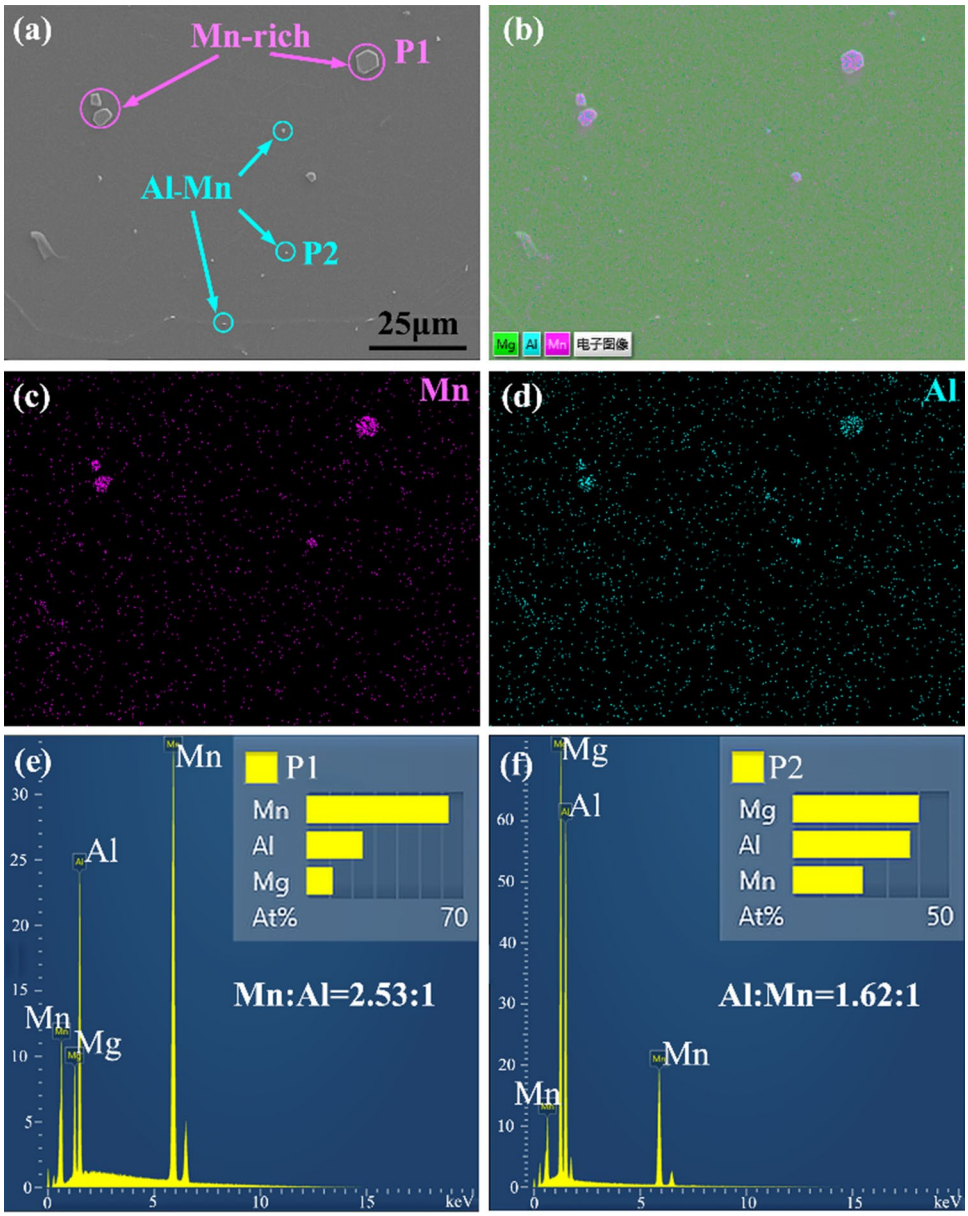


**Fig. 2** Morphology and element composition of precipitated phases in centrifugation casting alloy: **a** SEM, **b** EDS image, **c**, **d** Mn/Al element distribution maps and **e**, **f** atomic percentage of P1/P2 particles

**Table 2** The corresponding twinning systems in Fig. 6

| Twin system | Angle/axis of rotation | Matrix | Twins | Type |
|---|---|---|---|---|
| $\{10\bar{1}2\}10\bar{1}1$ | $86.3^{\circ}/11\bar{2}0$ | $M_1$ | $T_{11} \sim T_{16}$ | Tension |
| $\{10\bar{1}3\}30\bar{3}2$ | $64^{\circ}/11\bar{2}0$ | $M_5$ | $T_5$ | Compression |
| | | $M_2$ | $T_3$ | |
| $\{10\bar{1}1\}10\bar{1}2$ | $56^{\circ}/11\bar{2}0$ | $M_2$ | $T_{21}$ | |
| | | $M_6$ | $T_8$ | |
| $\{10\bar{1}1\} - \{10\bar{1}2\}$ | $38^{\circ}/11\bar{2}0$ | $M_2$ | $T_{22}, T_{23}$ | Secondary |
| | | $M_4$ | $T_4$ | |
| | | $M_6$ | $T_7$ | |
| $\{10\bar{1}3\} - \{10\bar{1}2\}$ | $22^{\circ}/11\bar{2}0$ | $M_5$ | $T_5$ | |
| | | $M_6$ | $T_6$,$T_9$ | |

As shown in Fig. 2, more dispersed precipitates rich in Mn and Al elements with uneven sizes were distributed in the matrix. These Al-Mn precipitates were mainly granular, irregularly block or elongated rod-like distributed within the

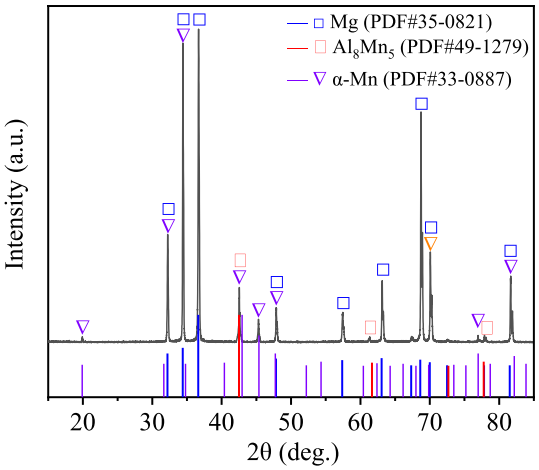


**Fig. 3** XRD analysis of the centrifugation casting alloy

α-Mg matrix or along grain boundaries. In which, the atomic ratio of Mn to Al elements in Mn-rich precipitates (P1) was nearly 2.53:1. Further experiments suggested that these large-sized Mn-rich particles were α-Mn elemental [22]. Meanwhile, the atomic ratio of Al to Mn elements in P2 particle was 1.62:1, which was close to that of $Al_8Mn_5$ phase. As shown in Fig. 3, the XRD analysis also confirmed that $Al_8Mn_5$ second phase and Mn elemental were the mainly precipitates in the centrifugation casting Mg–1.1Mn–0.5Al alloy.

The rolled Mg–1.1Mn–0.5Al alloys exhibited progressive plastic deformation characteristics with increasing strain, as shown in Fig. 4. When the sheets were rolled 1 pass to 0.2 strain, massive twins spread throughout the matrix. Most of these twins were distributed in banded bundles, accompanied by a variety of twin variants. These twin variants intercrossed each other to form a typical fragmentation morphology, with intersection angles of 50°–60°. Meanwhile, a few fine dynamic recrystallized (DRX) grains were formed around the twin intersection. As the cumulative strain was up to 0.4, abundant of subcrystalline structures spread throughout interior and boundaries of the twins and matrix. As a result, these twins and grains tended to concomitantly be decomposed into even finer DRXed grains. When the accumulated strain increased to 0.6, grain fragmentation became the dominant microstructure feature. Even more DRXed grains surrounded the initial grains, with a 30°–45° angle distribution along the rolling direction. Similar structures had been experimental confirmed, which were called the shear bands as typical features of rolled magnesium alloy [23]. With increasing strain to 0.8 through 7 passes rolling, these ubiquitous subgrain boundaries continued to incorporate the accumulated high-density dislocations and then transform into HAGBs, leading complete recrystallization.

The local misorientation, KAM and misorientation angle distributions of the rolled alloys are shown in Fig. 5. The maximum LAGBs frequency of the 2 passes rolled alloy was up to 75.34%. Then, with the increasing DRXed grains, the LAGBs frequency decreased gradually. However, due to higher strain rate, the HSRed Mg–1.1Mn–0.5Al alloys presented higher LAGBs frequency than as-extruded ($f_{LAGB} = 13.9\%$) or as-swaged Mg–0.6Mn–0.5Al–0.5Zn–0.4Ca alloys ($f_{LAGB} = 27.2\%$) [16]. These abundant LAGBs were suggested to impede dislocation slip, resulting in more lattice distortion and stress concentration [24]. Correspondingly, the GND density of the 2 passes rolled alloy increased to $6.25 \times 10^{14}$ $m^{-2}$, significantly higher than that of single pass rolled alloy ($3.11 \times 10^{14} m^{-2}$) and centrifugal casting alloy ($3.39 \times 10^{13} m^{-2}$). However, the increasing DRXed grains tended to absorb the nearby lattice dislocations, leading to the successive decrease of dislocation density in the 4 passes and 7 passes rolled alloys, with $\rho_{GND} = 4.78 \times 10^{14} m^{-2}$ and $\rho_{GND} = 4.14 \times 10^{14} m^{-2}$, respectively.

**Table 3** Mechanical performance of the Mg–1.1Mn–0.5Al alloys

| Samples | UTS (MPa) | YS (MPa) | FE(%) |
|---|---|---|---|
| Centrifugal cast | 197 ± 2 | 83 ± 1 | 12.4 ± 0.6 |
| 1 pass to 20% reduction | 264 ± 2 | 127 ± 2 | 14.4 ± 0.6 |
| 2 passes to 40% reduction | 317 ± 3 | 228 ± 2 | 14.2 ± 0.8 |
| 4 passes to 60% reduction | 343 ± 3 | 266 ± 2 | 16.3 ± 1.2 |
| 7 passes to 80% reduction | 378 ± 4 | 311 ± 3 | 20.4 ± 1.8 |

As shown in Fig. 6, the activated twin systems were marked with colored lines based on their misorientation angles, where the maximum deviation of the ideal axes and the corresponding misorientation angles were both set to 5°. The corresponding characteristics of the twin systems in Fig. 6 are shown in Table 2. The mass of $\{10\bar{1}2\}$, $\{10\bar{1}1\}$ and $\{10\bar{1}3\}$ primary twins, together with nearly equal number $\{10\bar{1}1\} - \{10\bar{1}2\}$ and $\{10\bar{1}3\} - \{10\bar{1}2\}$ double twins were distributed within the matrix intersecting or parallel to each other, becoming high-density dislocation plugging regions, which were distributed gray-black in the EBSD diffraction mass pattern. In addition, high strain was accumulated in several twins, resulting in difficult to be identified and taking on a gray color. Meanwhile, there were also some other uncommon twin systems, such as $\{10\bar{1}2\} - \{\bar{1}012\}$, $\{10\bar{1}2\} - \{01\bar{1}2\}$ and $\{10\bar{1}2\} - \{0\bar{1}12\}$ twin variants and so on. Compared with the conventional thermoplastic magnesium alloy [25–27], the HSRed Mg–1.1Mn–0.5Al alloy activated more deformation twinning systems, obtained a higher twinning fraction, and

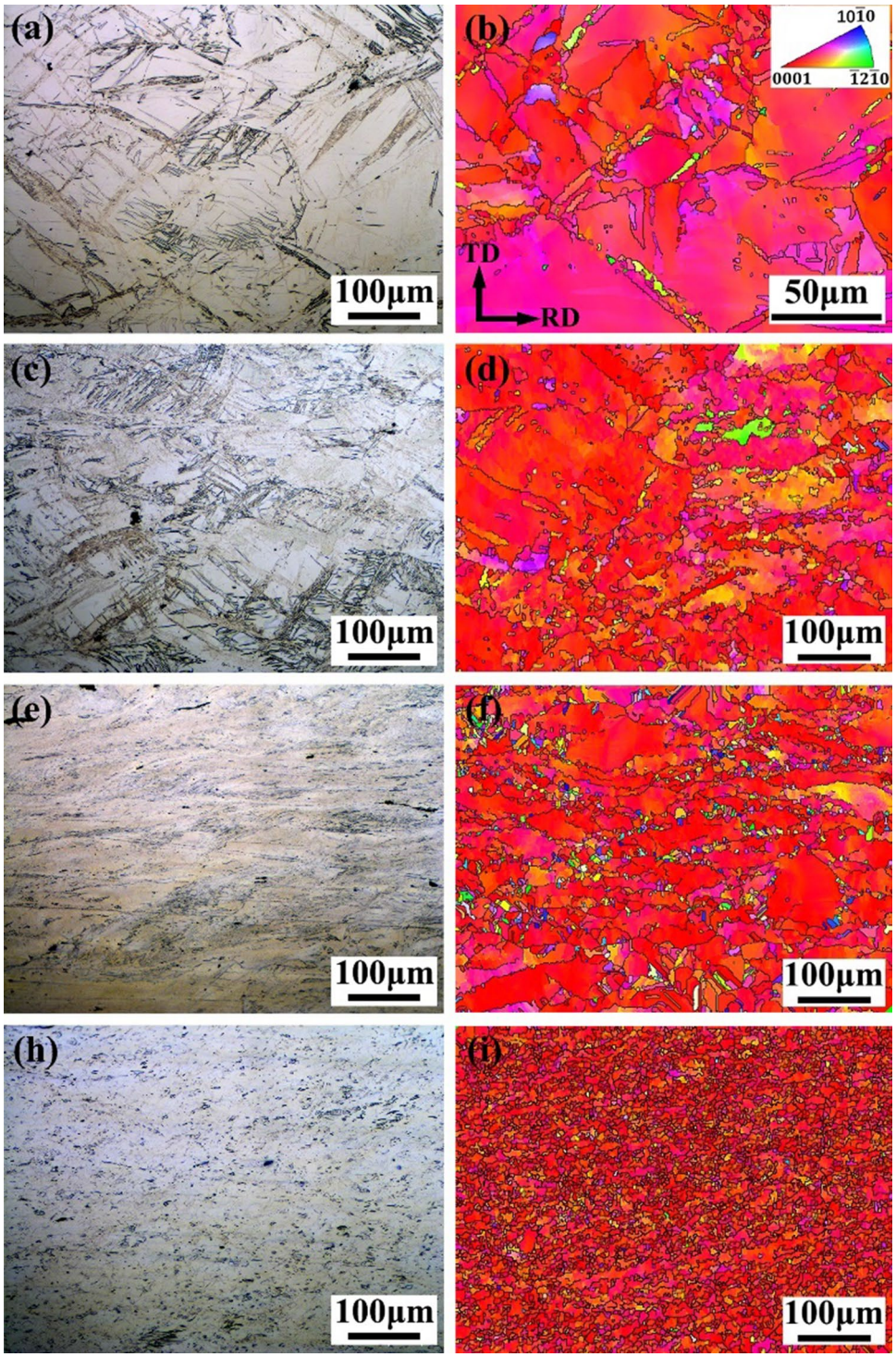


**Fig. 4** OM and EBSD IPF maps of the HSRed alloys after **a**, **b** 1 pass, **c**, **d** 2 passes, **e**, **f** 4 passes and **h**, **i** 7 passes rolling

promoted an even balanced distribution of the multiple system twins.

Figure 7 shows the recrystallization characteristics distribution and fraction of the 4 passes and 7 passes rolled alloys, in which the minimum misorientation angles to separate recrystallized, sub-structured, and deformed grains are 1 degree and 7.5 degree, respectively. Meanwhile, the color of fully recrystallized, sub-structured and deformed grains is defined by blue, yellow and red in sequence. With the increasing rolling pass, DRX dominated the plastic deformation of the rolled Mg–1.1Mn–0.5Al alloy. After 7 passes rolling to cumulative 80% reduction, the rolled alloys presented a fully DRX structure with significantly refined grain size of 4.72 μm. However, some DRXed

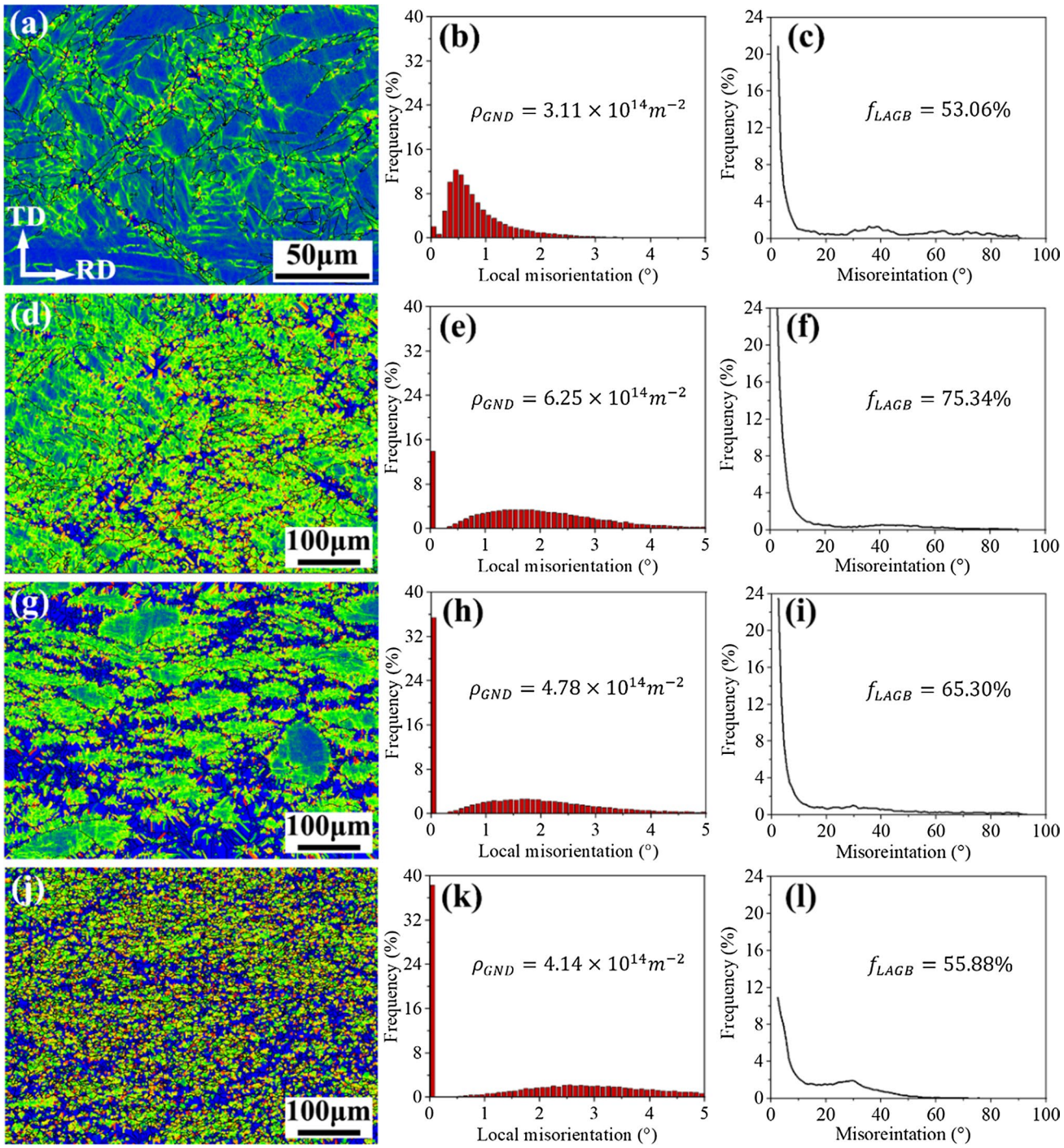


**Fig. 5** Local misorientation, KAM and misorientation angle distributions maps of the HSRed alloys after **a**, **b** and **c** 1 pass, **d**, **e** and **f** 2 passes, **g**, **h** and **i** 4 passes and **j**, **k** and **l** 7 passes rolling

grains retained massive LAGBs and thus appeared as substructures or deformed grains. In essence, DRX is a process in which plugging and accumulating dislocation slip, causing local stress concentration, driving lattice torsion, forming LAGBs and transforming into HAGBs. Hence, these residual LAGBs are the potential driving force for further refinement of DRXed grains.

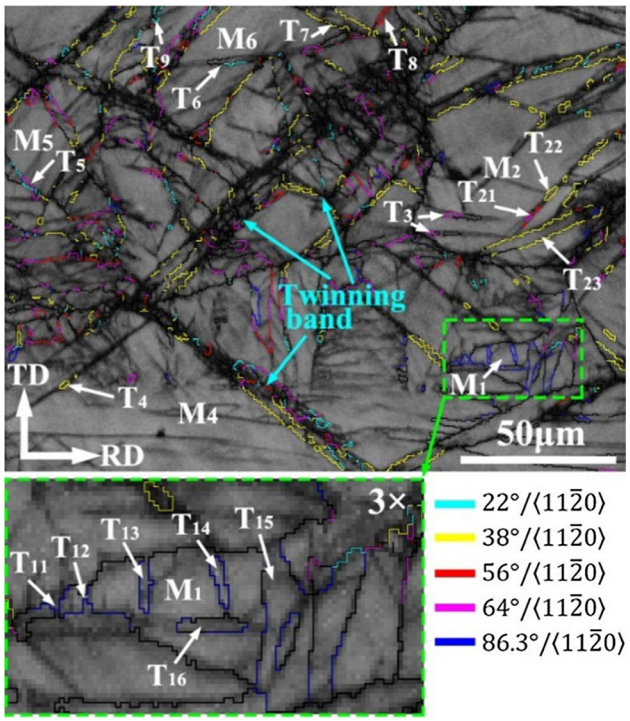


**Fig. 6** EBSD band contrast and marked twins of the HSRed Mg–1.1Mn–0.5Al alloy after 1 pass rolling

## 3.2 Mechanical Performance

Figure 8 shows the tensile stress–strain curves and mechanical properties of the centrifugal casting and the rolled Mg–1.1Mn–0.5Al alloys, compared with other rolled or extruded Mg–Mn–Al alloys. Meanwhile, the corresponding values of YS, UTS and FE are listed in Table 3. The tensile strength of the alloy increased synchronously with the increasing rolling pass. Ultimately, the rolled alloys by 7 passes to 80% cumulative reduction showed a highest YS of 311 MPa and UTS of 378 MPa. In addition, compared with other rolled or extruded Mg–Mn–Al alloy, the Mg–1.1Mn–0.5Al alloys through high strain rate rolling presented excellent strength-ductility synergy.

However, due to higher stress concentration, the ductility of the 2 passes rolled alloy decreased slightly compared with that of the single pass rolled alloy. Thereafter, the ductility increased significantly with the increasing rolling passes, thanks to the sharp decrease in average grain size with the increase of DRX fraction and the associated decrease of GND density.

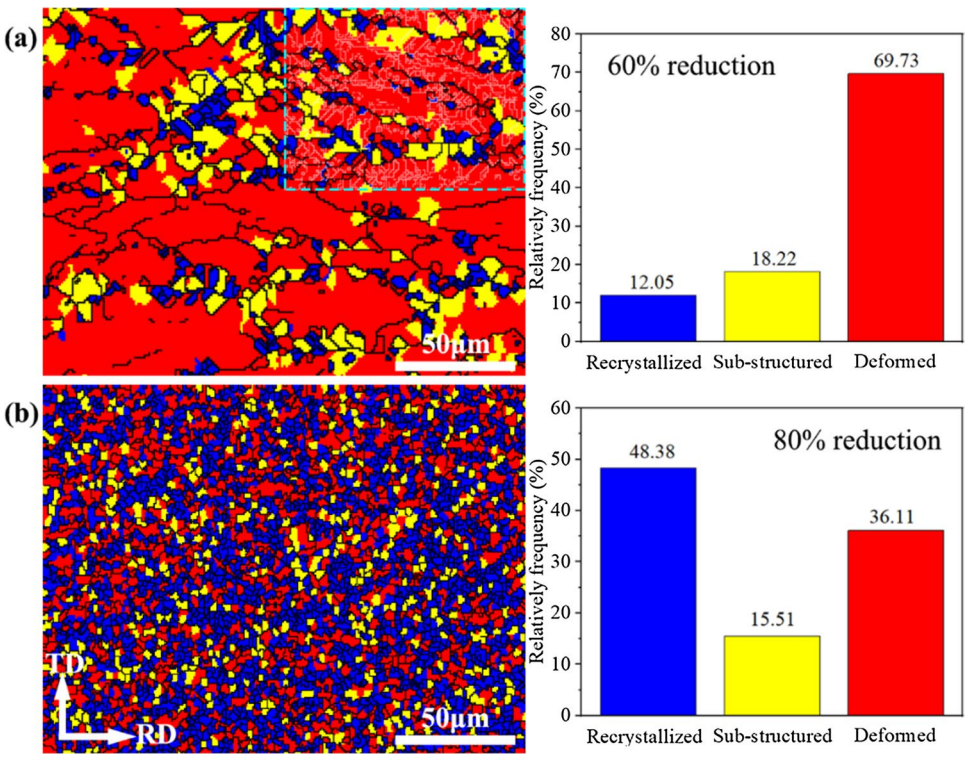


**Fig. 7** Dynamic recrystallization distribution and fraction of the HSRed alloys after **a** 4 passes and **b** 7 passes rolling

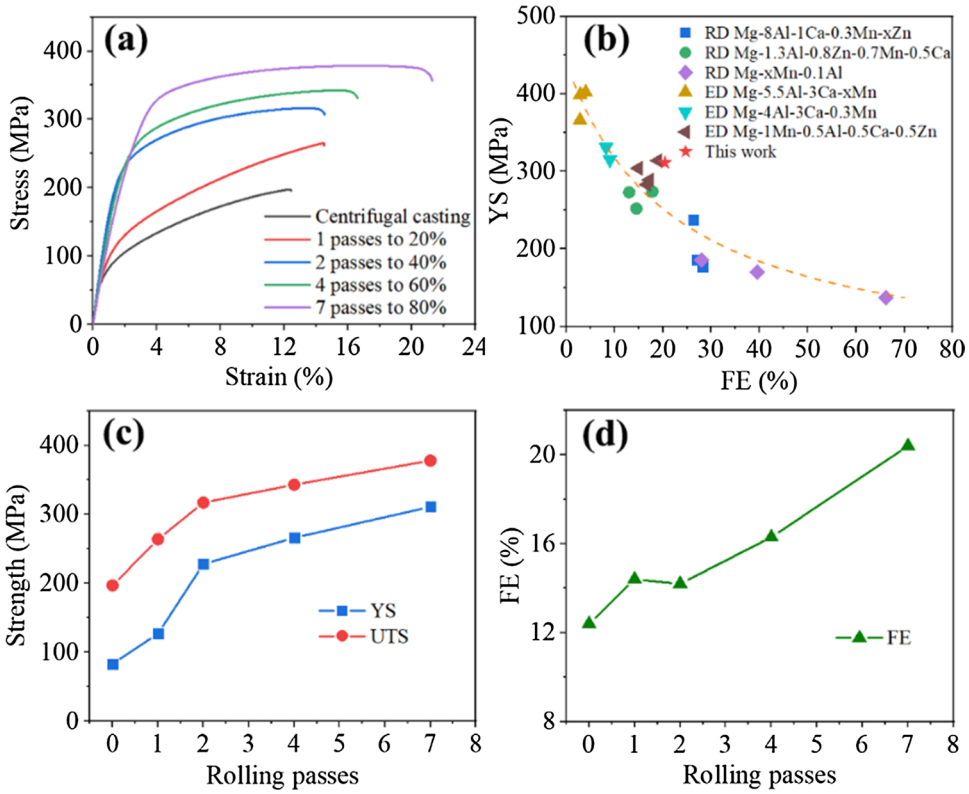


**Fig. 8** Mechanical properties of the Mg–1.1Mn–0.5Al alloys for **a** the tensile stress–strain curves, **b** comparison of YS and FE with other rolled (RD) or extruded (ED) Mg–Mn–Al alloys in references [28–33], variation trend of **c** YS, UTS and **d** FE

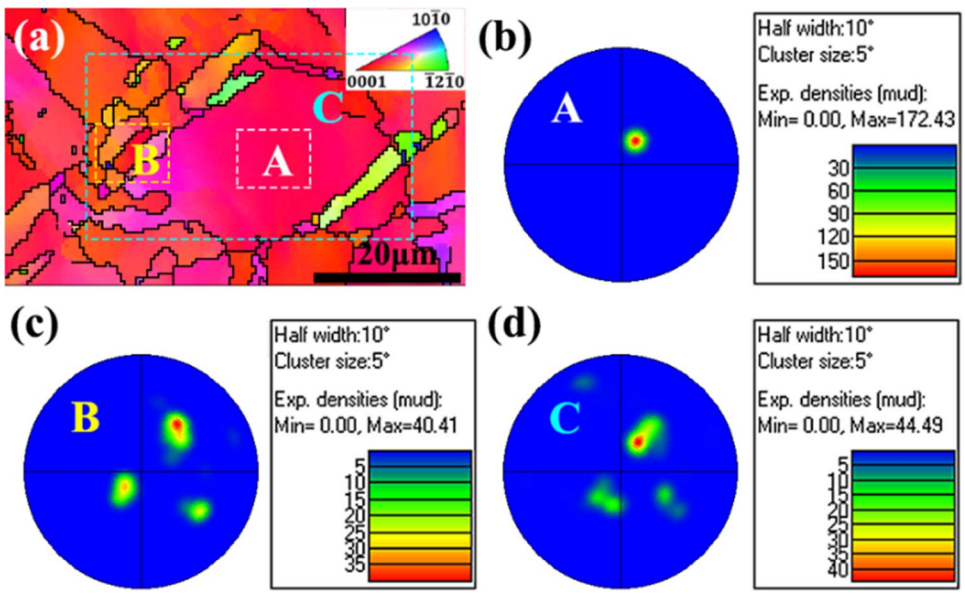


**Fig. 9** Twins weakening the {0001} texture in the 2 passes rolled alloys: **a** IPF map and the corresponding pole figure of **b** region A, **c** region B and **d** region C

## 4 Discussion

### 4.1 Effect of Twinning and Recrystallization on Basal Texture

As an essential strain coordination mechanism, deformation twinning is likely to be activated to coordinate the uniform plastic deformation at low temperature. Generally, high strain rolling at 473 K is not enough to activate sufficient slip systems, but promotes the nucleation and growth of deformation twins. Massive twin boundaries are more prone to accumulate dislocation and induce twinning dynamic recrystallization (TDRX) [23]. As shown in Figs. 4 and 5, more extensive dislocation slips and higher dislocation density lead to more DRXed grains with increasing cumulative deformation. Increasing dislocation density induces

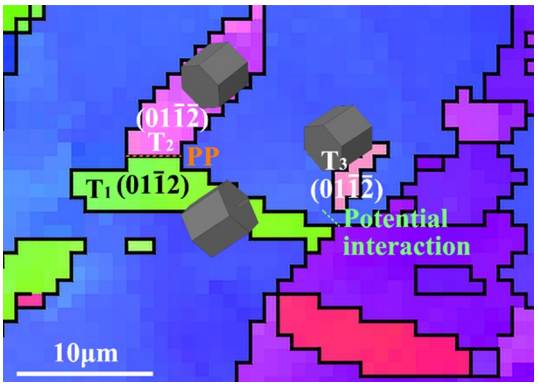


**Fig. 10** EBSD IPF map of TTB by coaxial {10$\bar{1}$2} twin interaction in the 2 passes rolled alloys

continuously. It has been evidenced that the activated twins, TDRX, DDRX and CDRX can lead to the orientation dispersion in basal texture or texture weakening in deformed Mg alloys [34–36].

As shown in Fig. 9, the misorientation of the twins in the 2 passes rolled Mg–1.1Mn–0.5Al alloys deflects relative to the matrix grains, resulting in the weakened {0001} basal texture. Furthermore, detwinning, double twinning or additional slip system can be activated during the plastic deformation of the twins, which can reduce the basal texture and asymmetry [37, 38]. Figure 10 shows that a common twinning boundary was formed when two coaxial {10$\bar{1}$2} twins interact. There are two possible common twinning boundary modes, basal/basal (BB) or prismatic/ prismatic intersection plane, due to the misorientation difference of the

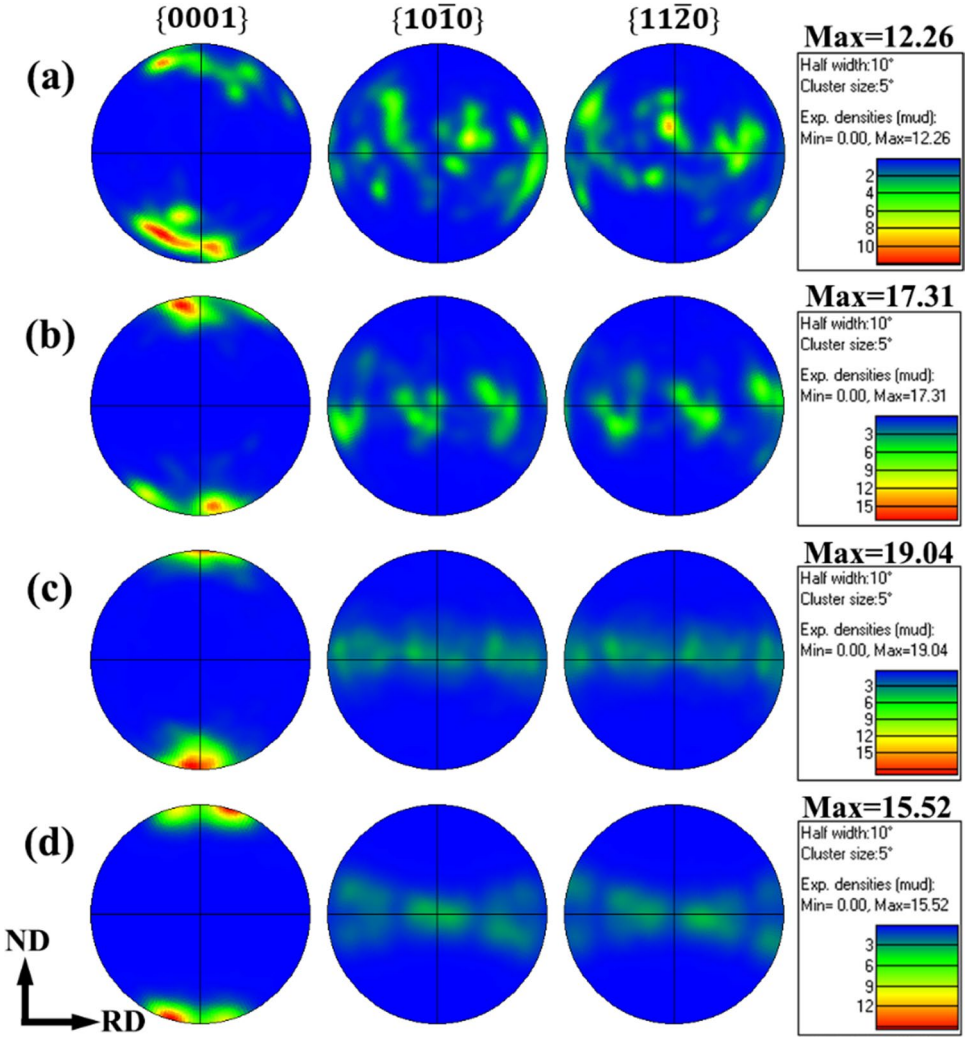


**Fig. 11** Pole figures of the HSRed alloys after **a** 1 pass, **b** 2 passes, **c** 4 passes and **d** 7 passes rolling

even more discontinuous dynamic recrystallization (DDRX) at grain boundaries and continuous dynamic recrystallization (CDRX) within deformation grains [6]. As a result, the DRXed grains fraction increases but the grain size decreases

coaxial {10$\bar{1}$2} tension twins [39]. The interaction structures formed between different twin variants facilitate the local strains coordination so as to improve the ductility.

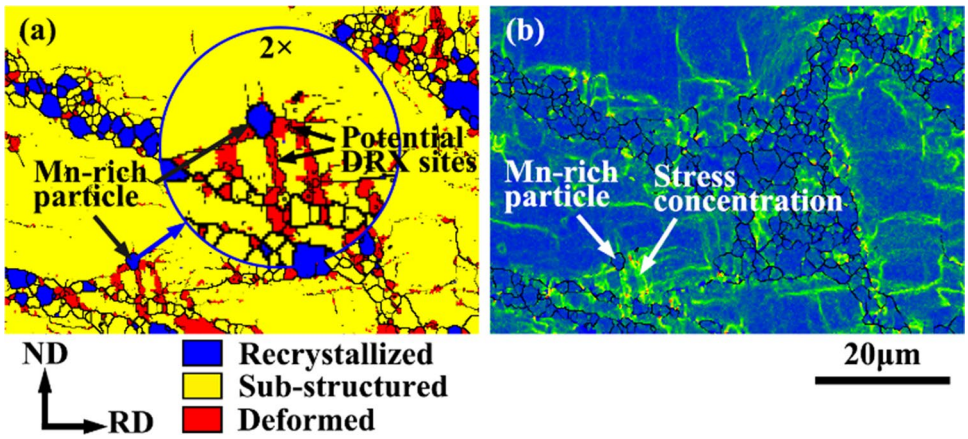


**Fig. 12** Particle stimulating nucleation in the 4 passes rolled alloy: **a** DRX and **b** KAM maps

However, the orientation shift of these deformed twins relative to the matrix does not offset the texture enhancement caused by the corresponding increase in strain. As shown in Fig. 11, the single pass rolled alloy presented an obvious (0001) basal texture with a maximum polar density value of 12.26. After 2 passes rolling, the maximum polar density of basal texture increased to 17.31. With 4 passes rolling to 0.6 strain, the maximum polar density was up to the peak of 19.04.

On the contrary, DRX is an effective method for texture weakening in deformed Mg alloys. As shown in Fig. 11d, the maximum pole density of 7 passes rolled alloy reduced to 15.52 due to the texture weakening effect of complete dynamic recrystallization. In particular, an unusual double-peak texture, where basal poles tilted about $\pm 20°$ away from ND to RD, was observed in the 7 passes rolled alloy. The published reports have evidenced that AZ31 magnesium sheets presented a c-axis//RD texture component and weak double-peak texture by means of equal channel angular rolling and subsequent continuous bending. After annealing, the texture finally became a typical double-peak texture, leading to significantly improved stretch formability [40]. The accumulated reduction of the cold rolled AZ31 sheets with similar double-peak texture was up to 39.2%, nearly double the 18.3% of the sheets with strong basal texture [41]. EBSD analysis confirmed that the tilt direction and rotation angle of the double-peak texture were exactly consistent with the tension twins [40]. In addition, there were also definite evidences that $\{10\bar{1}1\} - \{10\bar{1}2\}$ double twinning was the underlying induction factor in the formation of the double-peak texture [42]. Therefore, it can be inferred that twins are one of the important causes for the double-peak {0001} texture.

## 4.2 Alloying Elements and Precipitates

The first principles calculation recommends that the Mn element is beneficial to accelerate the dislocation propagation by pairing some partial dislocations in the atomic plane, and Al element helps to activate non-basal slips so as to coordinate the uniform plastic deformation in magnesium alloys [43]. Meanwhile, Mn element can effectively reduce the energy barrier of cross slip, resulting in more activated slip dislocations in magnesium alloys [12]. Nakata et al. [44] found that a large amount of high-density Gunier–Preston (G.P) zones appeared in the extruded Mg–0.3Al–0.3Ca alloy with added Mn element, which was conducive to the refinement of recrystallized grains.

In our study, an obvious dislocation plugging was observed around Mn-rich particles in rolled Mg–1.1Mn–0.5Al alloys, as shown in Fig. 12. This indicated that Mn-rich particles acted as a barrier to pinning dislocations. The local dislocation density concentration caused by dislocation pinning effect was conducive to induce sub-structured grains and recrystallized grains nearby. The orientation of the DRXed grains was more randomized that that of the primary grains, resulting in significantly weaker texture than the original deformed basal {0001} texture. This texture weakening is undoubtedly beneficial to reduce yield anisotropy and improve mechanical workability of the rolled Mg alloys at low temperature.

As previously mentioned, Mn increases significantly the critical resolved shear stress (CRSS) of basal slips of magnesium alloy, with an equivalent effect as the same content of Gd and Y rare earth elements [12]. Moreover, mass of nano-sized Al-Mn precipitates (~12 nm) are dispersed in the HSRed alloy, as shown in Fig. 13. These nanoparticles are proofed as $Al_8Mn_5$ precipitated phase to perform significant dispersion strengthening through pinning dislocations [13]. Due to the non-coherent relationship between Al-Mn particles and matrix grains, the precipitate strengthening can be calculated by Orowan strengthening mechanism [45]:

$$\sigma_{Orowan} = \frac{Gb}{2\pi\sqrt{1-v}} \bullet \frac{1}{\lambda} \bullet ln\left(\frac{D_p}{r_0}\right) \tag{3}$$

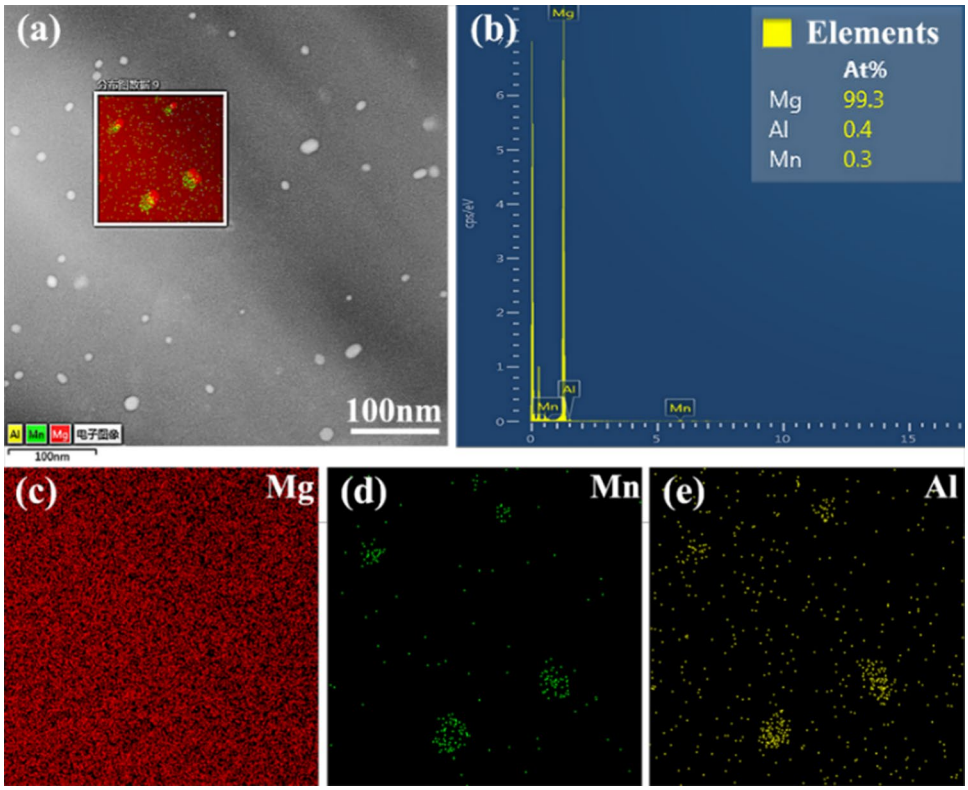


**Fig. 13** Elements distribution of the 7 passes rolled alloy: **a** STEM, **b** EDS, **c** Mg, **d** Mn and **e** Al elements

where $G$ is the shear modulus (~16.6 GPa), $b$ is the gliding dislocations Burgers vector (~0.32 nm), $v$ is Poisson ratio (~0.33), $\lambda$ is precipitated phase spacing taken by the line segment method (~76.9 nm), $r_0$ is dislocation core radius take as the modulus of Burgers vector and $D_p$ is the precipitate planar diameter (~12 nm). When the dislocation slips to the precipitates, the dislocation lines are blocked, resulting in arcing, extending, wrapping, reconnecting and forming the Orowan dislocation ring. According to the Orowan mechanism in Eq. 3, the more precipitates in unit volume, the better the effect of precipitation strengthening. In our study, the calculated precipitation strengthening contribution is 48.8 MPa, which is 15.7% of yield strength (~311 MPa) in the 7 passes rolled Mg-Mn-Al alloys.

### 4.3 Non-basal Slip Mediated Compressive Twin Strain Softening

Compared with the matrix grains, the $\{10\bar{1}1\}$ or $\{10\bar{1}3\}$ compression twins tend to form some lamellar "softening" regions, which are more prone to plastic deformation. Previous studies have suggested that the softening regions tend to be crack initiation zones, leading to premature material failure [46]. However, the high ductility of the HSRed Mg–1.1Mn–0.5Al alloy indicates that no premature cracks are formed in these softened regions. In fact, the primary reason why cracks tend to form in the compression twin region lies in the incongruity of the plastic deformation capacity between the harder matrix grains and the softened twin region. Thanks to mass of evenly distributed multisystem tension, compression and double twins, the HSRed Mg–1.1Mn–0.5Al alloy exhibits an overall softening characteristic, which is conducive to the improvement of ductility and workability.

Figure 14 shows the comparison of twin distribution and misorientation intensity of rolled Mg–1.1Mn–0.5Al alloy with different compression twin fraction, in which the color scheme of local misorientation in Fig. 14c, d was marked with rainbow band and the subgrain angle was definited as 5 degree with filter size of 3×3. Although both alloys consisted mainly of deformation twins rather than recrystallization, the types of mainly activated twins were significantly distinguished. When the rolling reduction was 10%, the proportional fraction of tension twins was significantly greater than that of compression twins and secondary twins. Meanwhile, although the corresponding average KAM value was only 0.8779, its peak intensity reached as high as 1.154. Nevertheless, the stress concentration pattern of marked regions 1–7 in Fig. 14 was not exactly the same. In regions 1–4 and 6, there were not only obvious regional stress concentration, but also some stress concentration sites (marked as red lines). In region 5 and 7, there was only a general regional stress concentration, but no obvious peak strength sites. However, in any case, these regions were stress concentration zones due to the dislocation slip barriers caused by the compression twin boundaries, which was not

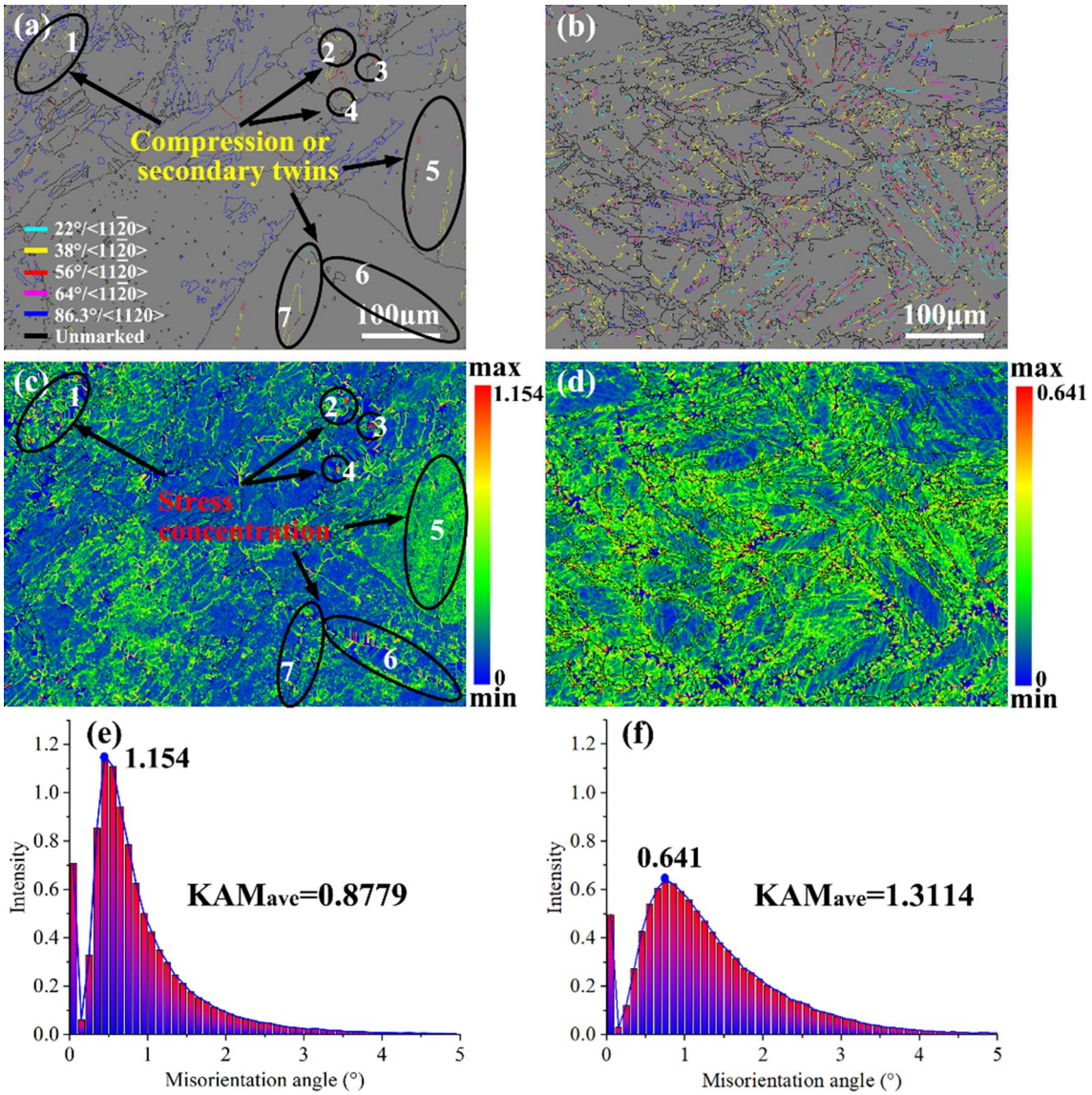


**Fig. 14** Comparison of twin distribution, local misorientation and misorientation intensity of the alloys: **a**, **c**, **e** with fewer compression and double twins while single pass rolled with 10% reduction and **b**, **d**, **f** with massive evenly distributed compression and double twins while single pass rolled with 20% reduction

common around the tension twins. Hence, when compression twins were relatively rare in the rolled Mg–1.1Mn–0.5Al alloy, extremely high-density dislocations were concentrated in the coarse matrix grains around the softening $\{10\bar{1}1\}$ compression twins and $\{10\bar{1}1\}-\{10\bar{1}2\}$ double twins, which caused a severe incompatibility of ductility between the compression twins, tension twins and matrix grains. In contrast, when massive compression twins and double twins spread throughout the rolled alloy with 20% reduction, the peak dislocation density were decreased sharply to 0.641 despite the average KAM value increased to 1.3114. This indicated that the potential for local crack initiation in compression twins and double twins would be greatly reduced. Therefore, it can be inferred that the softening effect of abundant evenly distributed compression twins is conducive to improving the ductility, rather than making it a crack source.

It has been generally believed that the non-basal slip of magnesium alloys is a thermal activation process. The plastic deformation mechanism of low temperature rolled magnesium alloys is dominated by basal slip and deformation twinning [47]. However, the only basal < a > slip is not sufficient to coordinate the high strain rolling deformation of the Mg–1.1Mn–0.5Al alloy. According to the "g·b = 0 invisible" dislocation extinction condition, the < c + a > dislocations are easily distinguished from basal < a > dislocations. Figure 15 shows that both basal < a > and

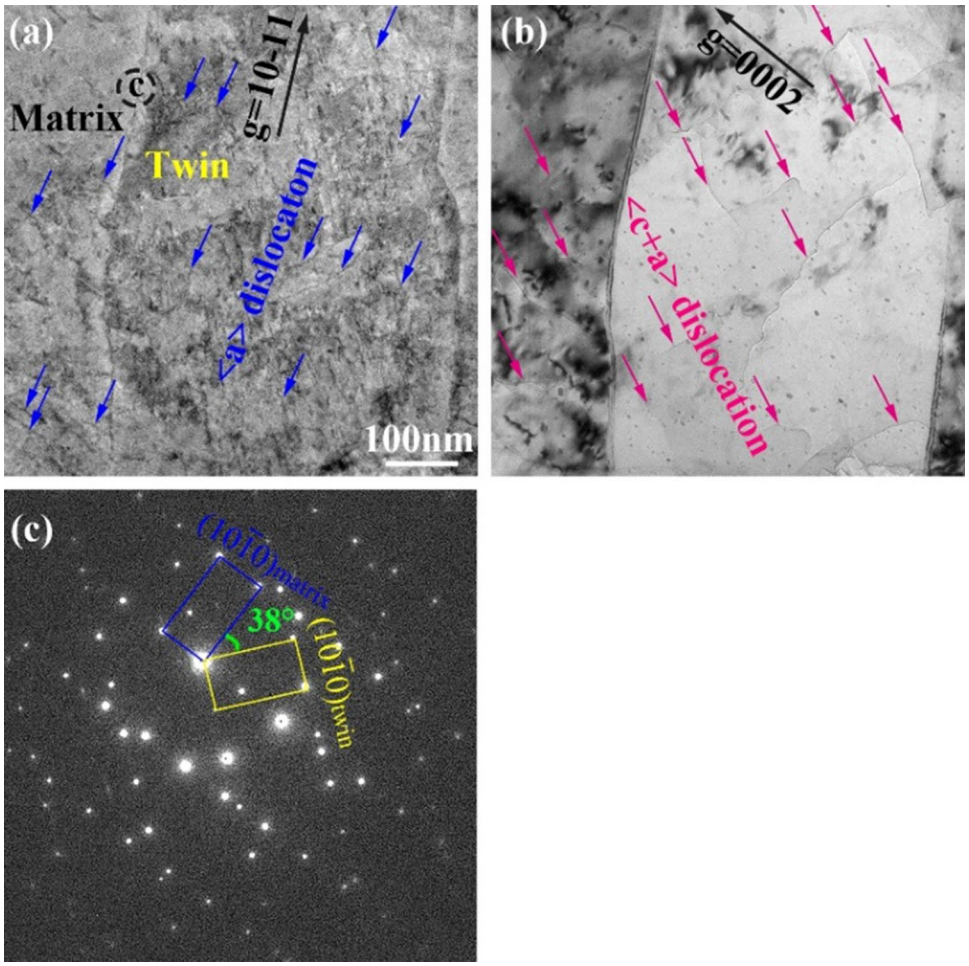


**Fig. 15** Dislocation morphology near a $\{10\bar{1}1\} - \{10\bar{1}2\}$ double twin in the 1 pass HSRed alloy under **a** $\vec{g} = 10\bar{1}1$ and **b** $\vec{g} = 0002$ beam conditions; **c** the diffraction spot at position c in picture **a**

non-basal < c + a > dislocations are activated in the matrix and twins of the rolled Mg–1.1Mn–0.5Al alloy. The Schmid factor (SF) of basal < a > dislocation in compression twins is generally several times larger than that of matrix [46], which makes it easier to activate more dislocation slips inside the twins. These activated basal < a > dislocations induce non-basal < c + a > dislocations lying in the strain coordination of the twinning interface, which facilitates uniform plastic deformation of the rolled alloys. Some studies suggest that the dislocation in the residual matrix is a < c > dislocation [46]. However, the forming of pure < c > dislocation in the HCP magnesium alloy must rely on the reaction of < a > and < c + a > dislocations.

Figure 16 shows the Schmid factor frequency distributions of the rolled alloys with different rolling passes. The SF of basal < a > and pyramidal II < c + a > slips of the single pass rolled alloy presents almost the same high value, but showing the opposite trends of regular decreasing and significant increasing after two passes rolling, respectively. Meanwhile, pyramidal I < c + a > slips showed higher SF values in all investigated alloys and increased even more significantly with the increasing rolling passes. These pyramidal < c + a > slip systems are more easily activated due to the high SF factor. The activation of these non-basal < c + a > slip systems greatly improve ductility and workability, which avoids crack initiation and material failure during the high strain rolling process of Mg–1.1Mn–0.5Al alloys. Thanks to the texture strengthening and fine-grain strengthening mediated by non-basal slips, the 7 passes rolled alloy with double-peak texture exhibits improved strength without loss of ductility. Huang et al. suggested that the double-peak texture was resulted from recrystallization and related to activated pyramidal < c + a > slips [48]. It has been proposed that recrystallization boundaries tend to absorb non-basal dislocations, resulting in rotation of the recrystallized grains. This rotation caused the ND-oriented fine recrystallized grains in the strong {0001} texture to be redirected approximate 20° towards RD direction [48]. Furthermore, each peak of this unusual texture component spread transversely a wider orientation, which is considered to be related to the activated pyramidal < c + a > slips [49].

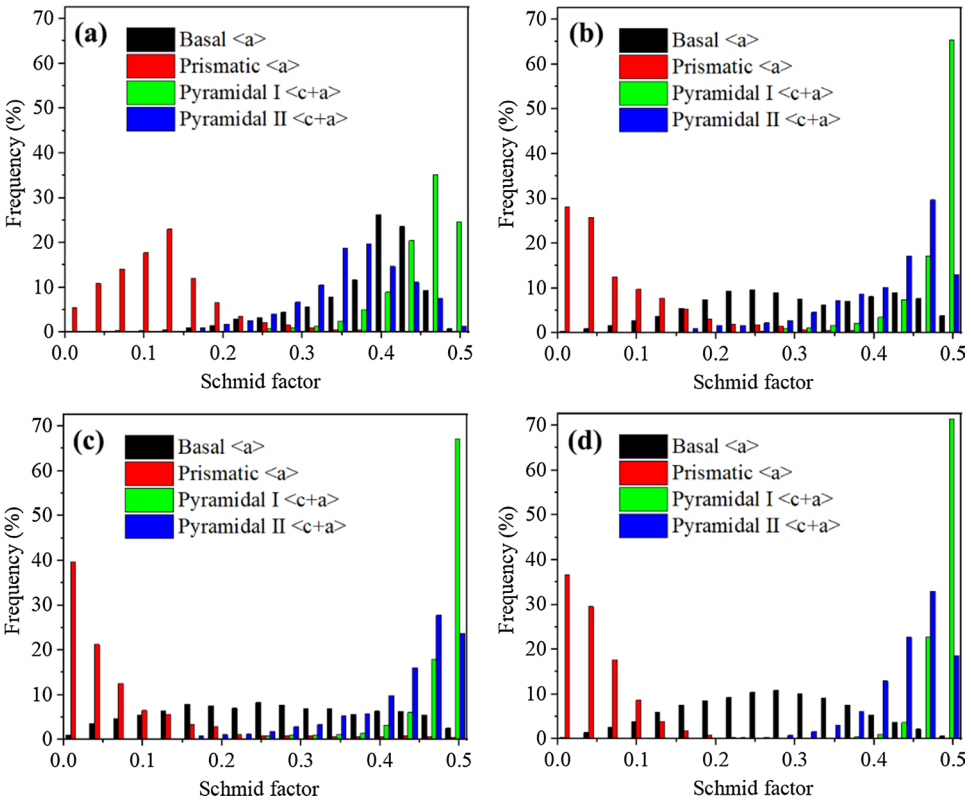


**Fig. 16** Schmid factor frequency distributions of the alloys after **a** 1 pass, **b** 2 passes, **c** 4 passes and **d** 7 passes rolling

## 5 Conclusions

The centrifugal casting Mg–1.1Mn–0.5Al alloys present admirable plastic workability, which helps to accept high strain rate rolling at low temperature. The excellent yield strength and ductility were obtained simultaneously via 7 passes rolling due to the activated non-basal slips, alloying elements and accelerated recrystallization. The main conclusions of our research are as following:

(1) Massive evenly distributed compression twins were formed in the rolled Mg–1.1Mn–0.5Al alloy with the high strain rate of 19.6–38.8 $s^{-1}$. Local strain coordination due to strain softening of sufficient compression twins contributes to the improvement of plasticity and workability rather than making it the cracks sources. This coordination and softening are important supporting measures for high strain rate rolling of Mg–1.1Mn–0.5Al alloy without cracking.

(2) The strength and ductility of the Mg–1.1Mn–0.5Al alloy after 7 passes rolling are synchronously improved due to the DRXed grains refinement strengthening, the LAGBs residual dislocation strengthening, the activated pyramidal < c + a > slips coordination, and the synergistic enhancement of Nano-sized Al-Mn precipitates on strength and plasticity. In which, the alloying elements of Mn and Al are considered to be brought out an activation of non-basal slip, allowing to acceptance of high strain rolling, and accelerated recrystallization.

(3) The large number of activated multiple twinning systems are mainly $\{10\bar{1}2\}$, $\{10\bar{1}1\}$, $\{10\bar{1}3\}$, $\{10\bar{1}1\}-\{10\bar{1}2\}$, $\{10\bar{1}3\}-\{10\bar{1}2\}$ and so on. These twins are roughly equal in proportion and evenly distributed, which is greatly beneficial for local strain coordination of twin-twin and twin-dislocation interactions.

(4) The activated dislocations are basal < a >, pyramidal I < c + a > and pyramidal II < c + a > slip systems. Prismatic < a > slips are difficult to be activated due to its lower SF. The strengthening and strain coordination of activated < c + a > dislocation slip, which is also beneficial to accelerate dynamic recrystallization, are important strengthening and toughening mechanisms for rolled Mg–1.1Mn–0.5Al alloys.

**Acknowledgements** The authors are grateful for the financial supports from the National Key R&D Program of China (No.2021YFB3701100), the National Natural Science Foundation of China (No.52271091).

**Data availability** No data was used for the research described in the article.

## Declarations

**Conflict of interest** The authors declare that they have no known competing financial interests or personal relationships that could have influenced the work reported in this paper.

## References


1. Y. Song, D. Liu, W. Tang, K. Dong, D. Shan, E.H. Han, J. Magn. Alloys **9**, 1220–1232 (2021)
2. A.P. Carvalho, R.B. Figueiredo, Adv. Eng. Mater. **24**, 2100846 (2022)
3. Z. Abbasi, R. Ebrahimi, J.M. Cabrera, Met. Mater. Int. **27**, 3983–3992 (2021)
4. S. Wang, W. Zhang, J. Yang, X. Jiao, J. Pan, G. Chu, Met. Mater. Int. **29**, 1195–1201 (2023)
5. X. Peng, W.-C. Liu, G.-H. Wu, Rare Met. **41**, 1176–1188 (2022)
6. F. Kong, Y. Yang, H. Chen, H. Liu, C. Fan, W. Xie, Heliyon. **8**, e09995 (2022)
7. Z. Ma, G. Li, Q. Peng, X. Peng, D. Chen, H. Zhang, J. Magn. Alloys **10**, 119–128 (2022)
8. D. Wang, M. Hu, S. Sugiyama, Z. Ji, H. Xu, Y. Wang, Results Phys. **15**, 102622 (2019)
9. R. Cheng, M. Li, S. Du, H. Pan, Y. Liu, M. Gao, Mater. Sci. Eng. A **786**, 139332 (2020)
10. K. Wang, J. Wang, X. Peng, S. Gao, H. Hu, L. Zeng, Mater. Sci. Eng. A **748**, 100–107 (2019)
11. J. She, F.S. Pan, W. Guo, A.T. Tang, Z.Y. Gao, S.Q. Luo, Mater. Des. **90**, 7–12 (2016)
12. Z. Wu, R. Ahmad, B. Yin, S. Sandlöbes, W.A. Curtin, Science **359**, 447–452 (2018)
13. L. Shao, C. Zhang, C. Li, A. Tang, J. Liu, Z. Yu, Mater. Charact. **183**, 111651 (2022)
14. P. Peng, X. He, J. She, A. Tang, M. Rashad, S. Zhou, Mater. Sci. Eng. A **766**, 138332 (2019)
15. T. Nakata, C. Xu, R. Ajima, K. Shimizu, S. Hanaki, T.T. Sasaki, Acta Mater. **130**, 261–270 (2017)
16. H. Chen, Y. Yang, F. Hu, X. Liu, F. Kong, X. Cui, Mater. Sci. Eng. A **865**, 144629 (2023)
17. X. Huang, M. Bian, I. Nakatsugawa, Y. Chino, M. Sato, K. Yamazaki, J. Alloys Compd. **887**, 161394 (2021)
18. M. Hao, W. Cheng, L. Wang, E. Mostaed, L. Bian, H. Wang, J. Magn. Alloys **8**, 899–909 (2020)
19. J. He, J. Chen, H. Yan, W. Xia, B. Su, P. Pan, J. Mater. Eng. Perform. **31**, 5201–5211 (2022)
20. Z. Yan, D. Wang, X. He, W. Wang, H. Zhang, P. Dong, Mater. Sci. Eng. A **723**, 212–220 (2018)
21. B. Balout, J. Litwin, J. Mater. Eng. Perform. **21**, 450–462 (2012)
22. H. Somekawa, D.A. Basha, A. Singh, Mater. Sci. Eng. A **766**, 138384 (2019)
23. F. Kong, W. Xie, G. Wei, Z. Ma, H. Chen, C. Fan, Mater. Sci. Technol. **39**, 283–299 (2023)
24. A. Jamali, A. Ma, J. Llorca, Scr. Mater. **207**, 114304 (2022)
25. L. Zhao, X. Guo, A. Chapuis, Y. Xin, Q. Liu, P. Wu, Metall. Mater. Trans. A **50**, 118–131 (2019)
26. S.-L. Ma, X.-Z. Tang, Q. Zu, Y.-F. Guo, Scr. Mater. **180**, 40–44 (2020)
27. W.Q. Chen, S. Deng, X.J. Zhao, S.N. Luo, J. Mater. Sci. Technol. **144**, 93–101 (2023)
28. M.Z. Bian, T.T. Sasaki, T. Nakata, Y. Yoshida, N. Kawabe, S. Kamado, Acta Mater. **158**, 278–288 (2018)
29. G.-l Gu, X.-n Ke, F.-p Hu, S.-j Zhao, G.-b Wei, Y. Yang, Trans. Nonferrous Met. Soc. China **32**, 483–492 (2022)
30. T. Nakata, C. Xu, K. Suzawa, K. Yoshida, N. Kawabe, S. Kamado, Mater. Sci. Eng. A **737**, 223–229 (2018)
31. Z.T. Li, X.G. Qiao, C. Xu, X.Q. Liu, S. Kamado, M.Y. Zheng, J. Alloys Compd. **836**, 154689 (2020)
32. P. Peng, J. She, A. Tang, J. Zhang, S. Zhou, M. Rashad, Mater. Sci. Eng. A **859**, 144229 (2022)
33. T. Homma, S. Hirawatari, H. Sunohara, S. Kamado, Mater Sci Eng, A. **539**, 163–169 (2012)
34. S.W. Lee, S.-H. Kim, W.-K. Jo, W.-H. Hong, W. Kim, B.G. Moon, J Alloys Compd. **791**, 700–710 (2019)
35. S.H. Lu, D. Wu, R.S. Chen, E.-h Han, J. Mater. Sci. Technol. **59**, 44–60 (2020)
36. X. Wang, P. Mao, R. Wang, Z. Liu, Z. Wang, F. Wang, Mater. Sci. Eng. A **772**, 138814 (2020)
37. B. Shi, C. Yang, Y. Peng, F. Zhang, F. Pan, J. Magn. Alloys **10**, 1476–1510 (2022)
38. Y. Xin, X. Zhou, Q. Liu, Mater. Sci. Eng. A **567**, 9–13 (2013)
39. Q. Sun, X.Y. Zhang, Y. Ren, L. Tan, J. Tu, Mater. Charact. **109**, 160–163 (2015)
40. D. Song, T. Zhou, J. Tu, L. Shi, B. Song, L. Hu, J. Mater. Process. Technol. **259**, 380–386 (2018)
41. X. Han, L. Hu, D. Jia, J. Chen, T. Zhou, S. Jiang, Z. Tian, The role of unusual double-peak texture in significant enhancing cold rolling formability of AZ31 magnesium alloy sheet. Trans. Nonferrous Met. Soc. (2022)
42. R. Zhu, C. Bian, Y. Wu, J. Mater. Eng. Perform. **26**, 2937–2946 (2017)
43. J. Zhang, Y. Dou, H. Dong, Scr. Mater. **89**, 13–16 (2014)
44. T. Nakata, C. Xu, Y. Matsumoto, K. Shimizu, T.T. Sasaki, K. Hono, Mater. Sci. Eng. A. **673**, 443–449 (2016)
45. M.R. Barnett, H. Wang, T. Guo, Int. J. Plast. **112**, 108–122 (2019)
46. M. Wang, C. Chen, Z. Zhang, R. Lei, F. Xia, Q. Lei, *Plastic Deformation Behaviors and Microstructural Evolution of FCC, BCC and HCP Metals* (Central South University Press, Changsha, 2021)
47. M.R. Barnett, Mater. Sci. Eng. A **464**, 1–7 (2007)
48. X. Huang, K. Suzuki, Y. Chino, M. Mabuchi, J. Alloys Compd. **537**, 80–86 (2012)
49. F. Guo, L. Liu, Y. Ma, L. Jiang, Y. Zhang, D. Zhang, J. Alloys Compd. **813**, 152117 (2020)